IEEE Access
Multidisciplinary | Rapid Review | Open Access Journal

Received 30 April 2023, accepted 18 May 2023, date of publication 2 June 2023, date of current version 14 June 2023.

Digital Object Identifier 10.1109/ACCESS.2023.3282428

RESEARCH ARTICLE

A Unified Grid-Forming and Grid-Following Primary Control Design With Optimized Enforcement of Grid Operational Constraints

SOUMYADEEP NAG, (Member, IEEE), ZHIHUA QU, (Fellow, IEEE), AND YING XU, (Member, IEEE)

Department of Electrical and Computer Engineering, University of Central Florida, Orlando, FL 32816, USA

Corresponding author: Zhihua Qu (qu@ucf.edu)

This work was supported in part by the U.S. Department of Energy under Award DE-EE0007998, Award DE-EE0009028, Award DE-EE0009152, and Award DE-EE0009339.

ABSTRACT A novel, unified control design is proposed for software-defined inverters (SDIs) to operate in either grid-forming (GFM) or grid-following (GFL) mode in AC grids/microgrids and to switch between the two modes seamlessly. The proposed GFM and GFL controls are systematically developed and analytically synthesized based on the dynamic state space models of the inverter, its output filters, and its terminal voltage and current at the AC grid/microgrid. The proposed GFM and GFL controls have, a) a nonlinear nominal output tracking control as the seed design, and b) a constraint-enforcing control. The GFM nominal control tracks frequency, voltage-magnitude, and angle, while the GFL nominal control tracks frequency as well as real and reactive power references. Tracking of either GFM or GFL output vector is ensured under the recursive Lyapunov design paradigm, naturally resulting in consistent current and voltage control laws. This paradigm allows the implementation of constraint-enforcing control that ensures that the frequency, voltage, power, and current injections dynamically satisfy their operational constraints in the presence of load variations and intermittent renewable power sources. Stability and convergence of the proposed GFM and GFL controls, and constraint enforcement are concluded analytically, and their effectiveness is demonstrated through simulations.

INDEX TERMS Grid-forming control, grid-following control, constraint-enforcing control, microgrid, phase angle control, frequency regulation, voltage regulation, power tracking, operational constraints.

I. INTRODUCTION

Grid forming (GFM) control has drawn tremendous research attention recently [1], [2], [3] as utilities add distributed energy resources (DERs) and aim for 100% renewable energy goals. Most of the existing grid-connected inverters are currently operated in the grid-following (GFL) mode, and they do not directly control the voltage or frequency of the grid. GFL inverters inject power into a well-established, stable AC system, and accordingly are sometimes referred to as 'free-riders' in terms of grid stability.

The associate editor coordinating the review of this manuscript and approving it for publication was Zhixiang Zou.

In a conventional inverter control design, two separate controls, referred to as voltage and current control loops, are chosen to be proportional-integral (PI) laws. The PI controls are not analytically derived but are tuned according to their operational conditions. In [4], [5], and [6] it is shown that, if the PI gains are tuned properly and droop curves are chosen appropriately, the droop-based controls can yield good transient responses under disturbances. To properly tune the control parameters, when there are many DERs in a large-scale power system, presents a significant challenge as the control gains and references tuned under one setting would vary with operating conditions.

There have been promising designs of unified GFM/GFL controls, in particular, direct nonlinear control designs. One

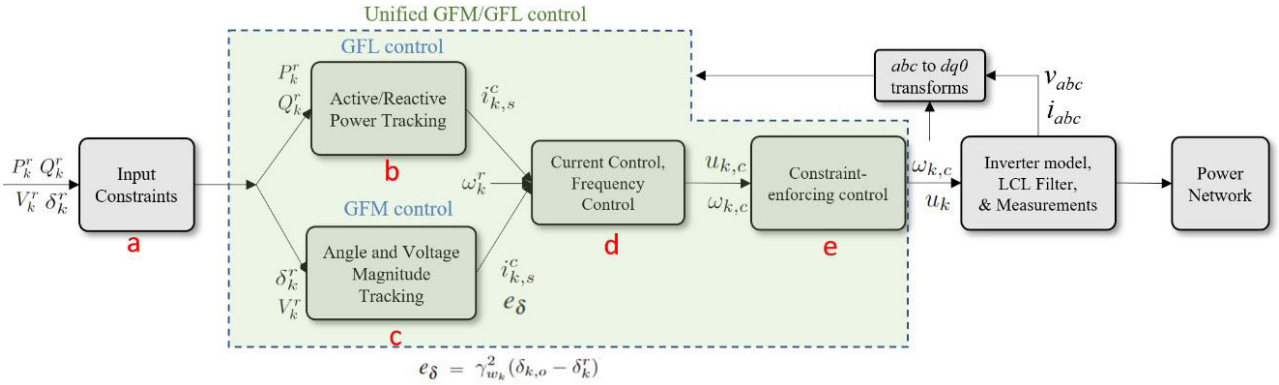

FIGURE 1. The proposed grid-form/grid-following primary control block diagram.

such design is the so-called virtual oscillator controller (VOC) [7], [8] using the oscillator synthesis theory [8], to achieve synchronization for parallelly-connected VOC inverters. A unified virtual oscillator controller design is proposed in [9], which enables a unified analysis, design, and implementation framework for both GFM and GFL. However, several issues such as the harmonic currents [10], [11] from the oscillators have been found. Also, DERs with VOC need to be further studied in the AC network. Alternatively, a direct Lyapunov design of state space GFM control is initiated in [12], and the basic framework is extended in this paper to allow both GFM and GFL controls as well as their transitions. More importantly, the Lyapunov design can enforce the grid operational constraints, which is a critical feature absent in all of the other approaches.

In this paper, we design controls that enable an SDI to operate in either the GFM mode or GFL mode as well as to switch between them, smoothly. Furthermore, the designed controls ensure operational constraints on frequency, voltage, power, and current injections are enforced in both operation modes. The proposed design is analytical and in a closed form in terms of the model of the inverter, its output filter, and the locally measurable voltage/current variables of the AC network [13]. The model-based analysis and design allow us to explicitly account for all the constraints of grid operation, and a constraint-enforcing control [14] is synthesized to dynamically meet all operational constraints. The unified GFM/GFL control works with nonlinearly designed secondary controls [15], [16], [17], [18], [19] which generate the voltage, angle, and frequency references by using a distributed subgradient method.

II. PROBLEM FORMULATION AND SYSTEM MODEL

The primary objective of the paper is to design unified control for software-defined inverters (SDIs) to operate in either GFM or GFL mode in AC grids/microgrids and to switch between the two modes. As shown in Fig. 1, the proposed control consists of five functional blocks:

- Block (a) imposes operational constraints on the following input signals received: reference voltage magnitude V_k^r, reference frequency ω_k^r. In addition, it also imposes DC power constraint P_{dc}^{max} as $P_{dc} \le P_{dc}^{max}$, which makes the control practical for distributed energy resources (DERs).
- Block (b) decides the current reference $i_{k,s}^c$ for GFL mode real power P_k^r and reactive power Q_k^r tracking control, while block (c) decides the current reference $i_{k,s}^c$ for GFM mode voltage reference V_k^r tracking control. Block (c) also computes the angle error in GFM mode, given the angle reference δ_k^r.
- Block (d) decides the reference signals $u_{k,c}$ for the inverter's PWM. It tracks the current references in either mode. Also, block (d) tracks frequency and angle for power sharing and synchronization in either mode.
- If any constraint is violated block (e) overrides the reference signals $u_{k,c}$ from block (d) to produce u_k. Block (e) performs an optimal projection of $u_{k,c}$ from block (d) onto the admissible set of $u_{k,c}$, such that voltage, current, active power, and reactive power constraints are obeyed in either mode. To meet the simpler constraints on frequency, a projection is built into the design of $\omega_{k,c}$.

To implement the designed controls, the three-phase measurements are transformed into the $dq0$ frame (which rotates with angular velocity $\omega_{k,c}$ and covers angular distance $\theta_k = \omega_{k,c}t = \omega_k t$). Specifically, for the kth inverter,

$$u_k \triangleq [u_{k,d}, u_{k,q}, u_{k,0}]^\top = T_{dq}(\theta_{k,c})u_{k,abc}(t),$$
$$i_{k,*} \triangleq [i_{k,*d}, i_{k,*q}, i_{k,*0}]^\top = T_{dq}(\theta_{k,c})i_{k,*,abc}(t),$$
$$v_{k,*} \triangleq [v_{k,*d}, v_{k,*q}, v_{k,*0}]^\top = T_{dq}(\theta_{k,c})v_{b,*,abc}(t),$$

where $*$ denotes the specific location in the circuit, subscripts d, q and 0 denote the corresponding d component, q component, and 0 component, respectively; and the $dq0$ transformation matrix is given by

$$T_{dq0}(\theta_{k,c}) = \frac{2}{3}\begin{bmatrix} \sin(\theta_{k,c}) & \sin(\theta_{k,c}-\frac{2\pi}{3}) & \sin(\theta_{k,c}+\frac{2\pi}{3}) \\ \cos(\theta_{k,c}) & \cos(\theta_{k,c}-\frac{2\pi}{3}) & \cos(\theta_{k,c}+\frac{2\pi}{3}) \\ \frac{1}{2} & \frac{1}{2} & \frac{1}{2} \end{bmatrix}.$$

Once the control $u_{k,c}$ is designed, the control output to the PWM generator of the inverter is the three-phase time function provided by

$$u_{k,abc}(t) = T_{dq0}^{-1}(\theta_{k,c})[u_{k,d}, u_{k,q}, u_{k,0}]^\top.$$

In the rest of this paper, the 0 component has been neglected as the power system is assumed to be balanced for simplicity of derivations.

A. MODELS OF SDI, OUTPUT FILTER, AND POWER NETWORK

To illustrate the proposed control design, we choose to use the following simplified dynamic model of the inverter in the analytical derivations:

$$v_{k,s} = \frac{v_{k,dc}}{2}u_k, \tag{1}$$
$$\dot{\delta}_{k,o} = \omega_k - \omega_0, \tag{2}$$
$$\omega_k = \omega_{k,c}, \tag{3}$$

where $\omega_{k,c}$, $v_{k,s}$, $\delta_{k,o}$ and u_k are the frequency control signal, the switching voltage output, and the phase angle and the voltage control input in the $dq0$ frame. In other words,

$$v_{k,s} = \begin{bmatrix} v_{k,sd} \\ v_{k,sq} \end{bmatrix}, \quad u_k = \begin{bmatrix} u_{k,d} \\ u_{k,q} \end{bmatrix}.$$

Should a dynamic model of inverter's electromagnetic transient (EMT) be available as illustrated in [20] and [21], the proposed design method can be readily applied by incorporating the model into the design via the standard recursive design process [22], [23].

The inverter and its output LCL filter are shown in Fig. 2. For the kth SDI, its output LCL filter has the following vector-form, state-space model in the $dq0$-frame:

$$\frac{di_{k,o}}{dt} = A_{k,11}i_{k,o} + A_{k,12}v_{k,o} + D_{k,1}v_{k,b} \tag{4}$$
$$\frac{dv_{k,o}}{dt} = A_{k,21}i_{k,o} + A_{k,22}v_{k,o} + A_{k,23}i_{k,s} \tag{5}$$
$$\frac{di_{k,s}}{dt} = A_{k,32}v_{k,o} + A_{k,33}i_{k,s} + B_{k,3}u_k, \tag{6}$$

where

$$i_{k,s} = [i_{k,sd} \quad i_{k,sq}]^\top, \quad v_{k,o} = [v_{k,od} \; v_{k,oq}]^\top,$$
$$i_{k,o} = [i_{k,od} \; i_{k,oq}]^\top, \quad u_k = [u_{k,d} \; u_{k,q}]^\top,$$
$$A_{k,11} = \begin{bmatrix} -\frac{R_{k,c}}{L_{k,c}} & \omega_k \\ -\omega_k & -\frac{R_{k,c}}{L_{k,c}} \end{bmatrix}, \quad A_{k,12} = \frac{1}{L_{k,c}}I_{2\times 2},$$
$$A_{k,21} = -\frac{1}{C_{k,f}}I_{2\times 2}, \qquad A_{k,22} = \begin{bmatrix} 0 & \omega_k \\ -\omega_k & 0 \end{bmatrix},$$
$$A_{k,32} = -\frac{1}{L_{k,f}}I_{2\times 2}, \qquad A_{k,33} = \begin{bmatrix} -\frac{R_{k,f}}{L_{k,f}} & \omega_k \\ -\omega_k & -\frac{R_{k,f}}{L_{k,f}} \end{bmatrix},$$
$$D_{k,1} = -A_{k,12}, \quad A_{k,23} = -A_{k,21}, \quad B_{k,3} = -\frac{v_{k,dc}}{2}A_{k,32}.$$

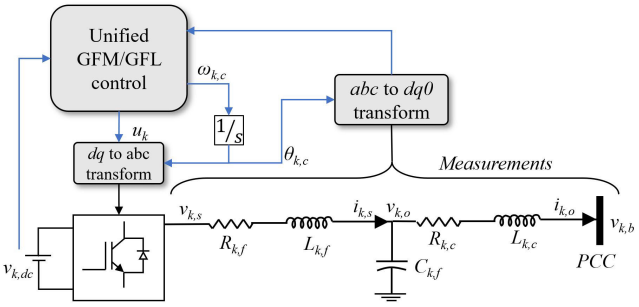

FIGURE 2. Inverter and filter model showing measurements.

The output voltage magnitude and the instantaneous active and reactive powers of each inverter are the critical variables defined as follows:

$$V_{k,o} = \|v_{k,o}\|, \tag{7}$$
$$P_k = \frac{3}{2}(v_{k,od}i_{k,od} + v_{k,oq}i_{k,oq}) = \frac{3}{2}i_{k,o}^\top v_{k,o}, \tag{8}$$
$$Q_k = \frac{3}{2}(v_{k,oq}i_{k,od} - v_{k,od}i_{k,oq}) = \frac{3}{2}i_{k,o}^\top H_q v_{k,o}, \tag{9}$$

where $H_q = \begin{bmatrix} 0 & 1 \\ -1 & 0 \end{bmatrix}$. The variables used in (4) through (6) correspond to those in Fig. 2, where PCC is the point of common coupling to the external power network. It follows from (4) to (6) that the outputs $V_{k,o}$, P_k, and Q_k each have a relative degree of two; please see [22] for the definition of relative degree.

B. OPERATIONAL CONSTRAINTS

One of the unique features of the designed controls is that the whole state and output vectors can meet their operational constraints simultaneously.

The frequency and voltage constraints on the SDI operation are:

$$\omega_k \in [\omega_0(1-\Delta_\omega), \; \omega_0(1+\Delta_\omega)] \triangleq [\underline{\omega}, \; \overline{\omega}] \tag{10}$$
$$V_{k,o} \in [V_0(1-\Delta_V), \; V_0(1+\Delta_V)] \triangleq [\underline{V}, \; \overline{V}], \tag{11}$$
$$|v_{k,sq}| \le \frac{2V_0\epsilon_v}{v_{k,dc}} \tag{12}$$

where $\epsilon_v > 0$ is a design parameter of q-axis voltage, Δ_ω and $\Delta_V > 0$ are the maximum tolerance of frequency and voltage derivations (typically 5%), respectively. $\epsilon_v > 0$ being a very small quantity ensures near-perfect grid voltage orientation of the dq-frame at all times.

The current limits $\overline{I}_k$ is the rated value of the SDI:

$$I_{k,s} = \|i_{k,s}\| \le \overline{I}_k, \tag{13}$$

and the SDI's output power constraints are denoted by

$$\underline{P}_k(t) \le P_k \le \overline{P}_k(t) \tag{14}$$
$$-\overline{Q}_k(t) \le Q_k \le \overline{Q}_k(t) = \sqrt{\overline{S}_k^2 - P_k^2(t)}. \tag{15}$$

For PV inverters, $\overline{P}_k(t) = P^*_{k,dc}(t)$, where $P^*_{k,dc}(t)$ is the DC power output under MPPT control, and $\underline{P}_k(t) = 0$. For storage devices, $\underline{P}_k(t)$ can assume a negative value.

III. GRID-FORMING PRIMARY CONTROL DESIGN

In this section, state-space tracking controls of angle, frequency, and voltage are designed to account for the dynamic coupling between frequency and voltage/current.

A. PRIMARY CONTROL FOR ANGLE AND FREQUENCY TRACKING

The frequency tracking controller's output, denoted by $\omega_{k,c}$, aims to make ω_k and $\delta_{k,o}$ track ω^r_k and δ^r_k, respectively, while satisfying constraint (10). If the control $\omega_{k,c}$ is chosen in the form of

$$\begin{aligned}\omega_{k,c} &= \mathrm{SAT}_{[\underline{\omega},\,\overline{\omega}]}\left(\hat{\omega}_{k,c}\right),\\ \hat{\omega}_{k,c} &= \omega_0 - \int_{t_{k,0}}^{t} [2\gamma_{w_k}(\omega_k - \omega^r_k) + \gamma^2_{w_k}(\delta_{k,o} - \delta^r_k)]dt\end{aligned} \tag{16}$$

any given reference angle and frequency, δ^r_k and ω^r_k satisfying inequality (10), are effectively and asymptotically tracked. Here γ_{w_k} is a small positive gain, and $\mathrm{SAT}_{[\underline{\omega},\,\overline{\omega}]}$ is the saturation function with the limits $\underline{\omega}/\overline{\omega}$. To understand the stability of the designed control (16), we see from (3) and (16) that

$$\begin{aligned}\ddot{\delta}_{k,o} &= \frac{d}{dt}(\omega_{k,c} - \omega_0)\\ &= -2\gamma_{w_k}(\omega_k - \omega^r_k) - \gamma^2_{w_k}(\delta_{k,o} - \delta^r_k)\\ &= -2\gamma_{w_k}\dot{\delta}_{k,o} - \gamma^2_{w_k}(\delta_{k,o} - \delta^r_k) - 2\gamma_{w_k}(\omega_0 - \omega^r_k),\end{aligned}$$

which shows critically-damped asymptotic convergence provided that ω^r_k converges to ω_0, if γ_{w_k} is selected properly. This ensures that the required angle is tracked while satisfying operational constraint (10) on frequency.

B. VOLTAGE TRACKING CONTROL

The phase angle $\delta_{k,o}$ is controlled by (16) so it can track its reference δ^r_k, and consequently the d-axes of the inverter voltage $u_{k,d}$ is always in phase with $v_{k,o}$. With the references of the phase angle and magnitude determined, we can set $v^r_{k,oq} = 0$ and hence have

$$v^r_{k,o} = \begin{bmatrix} v^r_{k,od} \\ v^r_{k,oq}\end{bmatrix} = \begin{bmatrix} V^r_k \\ 0\end{bmatrix}. \tag{17}$$

Suppose that the reference output voltage vector $v^r_{k,o}$ is set by (17). Then, $v^r_{k,o}$ can be tracked by $v_{k,o}$ under the voltage tracking control $u_{k,c} = u_{k,v}$, where

$$\begin{aligned}u_{k,v} = -B^{-1}_{k,3}\Big[&A_{k,32}v_{k,o} + A_{k,33}i_{k,s}\\ &+ \gamma_{k,is}(i_{k,s} - i^c_{k,s}) - \frac{di^c_{k,s}}{dt}\Big],\end{aligned} \tag{18}$$

$\gamma_{k,vo}, \gamma_{k,is} > 0$ are control gains, and

$$\begin{aligned}i^c_{k,s} = -A^{-1}_{k,23}\Big[&A_{k,21}i_{k,o} + A_{k,22}v_{k,o}\\ &+ \gamma_{k,vo}(v_{k,o} - v^r_{k,o}) - \frac{dv^r_{k,o}}{dt}\Big],\end{aligned} \tag{19}$$

$$\begin{aligned}\frac{di^c_{k,s}}{dt} = -A^{-1}_{k,23}\Big[&A_{k,21}\frac{di_{k,o}}{dt}\\ &+ (A_{k,22} + \gamma_{k,vo})\frac{dv_{k,o}}{dt} - \frac{d^2v^r_{k,o}}{dt^2}\Big].\end{aligned} \tag{20}$$

Here $di_{k,o}/dt$ and $dv_{k,o}/dt$ are given by (4) and (5), respectively. To understand the stability of the designed control, consider

$$e_{vo} = v_{k,o} - v^r_{k,o}; \quad \dot{e}_{vo} = \dot{v}_{k,o} - \dot{v}^r_{k,o}$$

and

$$e_{is} = i_{k,s} - i^c_{k,s}; \quad \dot{e}_{is} = \dot{i}_{k,s} - \dot{i}^c_{k,s}.$$

First, substituting u_k from (18) in (6) transforms (6) into

$$\dot{e}_{is} = -\gamma_{k,is}e_{is},$$

which shows first order convergence of e_{is} to 0. Similarly, substituting $i^c_{k,s}$ from (19) in (5) transforms (5) into

$$\dot{e}_{vo} = -\gamma_{k,vo}e_{vo},$$

which similarly shows first-order convergence of e_{vo} to 0, given that e_{is} converges faster than e_{vo} to 0. To facilitate the faster convergence of e_{is} to 0 we consider $\gamma_{k,is} > \gamma_{k,vo}$. Thus, the feedback structure [23] allows us to conclude asymptotic stability for first e_{is} and then e_{vo}. One might argue that this form of control requires derivatives. Note, that since the time steps for the inverter controls are in the order of micro-seconds, the value of these derivatives can be ignored. However, considering this argument and substituting (18) and (19) without the derivatives into the system equations, (6) and (5)

$$\dot{v}_{k,o} + \gamma_{k,vo}v_{k,o} = \gamma_{k,vo}v^r_{k,o}$$

and

$$\dot{i}_{k,s} + \gamma_{k,is}i_{k,s} = \gamma_{k,is}i^c_{k,s}$$

that $i_{k,s}$ and $v_{k,o}$ converge onto their respective references of $i^c_{k,s}$ and $v^r_{k,o}$.

IV. NON-LINEAR GRID-FOLLOWING CONTROL

In this section, a non-linear recursive primary tracking control strategy is designed for GFL mode of the SDI. This design uses identical design logic and involves the same control blocks as the GFM controls. The only difference lies in the manner in which the current references are generated. This enables the unification of GFM and GFL controls.

A. WITH POWER FEEDBACK

Similar to the voltage controller, the power injection references P_k^r and Q_k^r can be tracked by P_k and Q_k respectively if $u_{k,pq}$ is chosen as,

$$u_{k,pq} = -B_{k,3}^{-1}\Big[A_{k,32}v_{k,o} + A_{k,33}i_{k,s} + \gamma_{k,is}(i_{k,s} - i_{k,s}^c) - \frac{di_{k,s}^c}{dt}\Big], \quad (21)$$

where $\gamma_{k,is} > 0$ is a control gain, and

$$i_{k,s}^c = -G_{k,pq}^{-1}\left\{F_{k,pq} + \gamma_{k,pq}e_{pq}\right\}, \quad (22)$$

where

$$e_{pq} = \left[(P_k - P_k^r)\,(Q_k - Q_k^r)\right]^\top \quad (23)$$

$$F_{k,pq} = \frac{3}{2}\begin{bmatrix} v_{k,o}^\top \\ v_{k,o}^\top H_q^\top \end{bmatrix}(A_{11}i_{k,o} - A_{12}A_{22}^{-1}(A_{21}i_{k,o} - \dot{v}_{k,o}) + D_1 v_{k,b}) + \frac{3}{2}\begin{bmatrix} i_{k,o}^\top \\ i_{k,o}^\top H_q \end{bmatrix}\dot{v}_{k,o}, \quad (24)$$

$$G_{k,pq} = -\frac{3}{2}\begin{bmatrix} v_{k,o}^\top \\ v_{k,o}^\top H_q^\top \end{bmatrix}A_{12}A_{22}^{-1}A_{23}. \quad (25)$$

To understand the stability of the proposed control, consider the following. If we have

$$\dot{e}_{pq} = \frac{3}{2}\begin{bmatrix} v_{k,o}^\top \\ v_{k,o}^\top H_q^\top \end{bmatrix}\dot{i}_{k,o} + \frac{3}{2}\begin{bmatrix} i_{k,o}^\top \\ i_{k,o}^\top H_q \end{bmatrix}\dot{v}_{k,o}, = F_{k,pq} + G_{k,pq}i_{k,s} \quad (26)$$

from (8) and (9). Let $e_{is} = i_{k,s} - i_{k,s}^c$. Using the definition of $i_{k,s}$ and $i_{k,s}^c$ from (26) and (22), respectively, we have

$$\dot{e}_{pq} = -\gamma_{k,pq}e_{pq} + G_{k,pq}e_{is}$$

Substituting (21) into (6) we have,

$$\dot{e}_{is} = -\gamma_{k,is}e_{is}$$

Choosing $i_{k,s}^c$ as (22) guarantees that e_{is} converges to 0, following which, e_{pq} asymptotically converges to 0 for any choices of $\gamma_{k,pq}$, $\gamma_{k,is} > 0$ such that $\gamma_{k,pq} < \gamma_{k,is}$.

Control (21) requires $di_{k,s}^c/dt$ which is given by

$$\frac{di_{k,s}^c}{dt} = G_{k,pq}^{-1}\dot{G}_{k,pq}G_{k,pq}^{-1}[F_{k,pq} + \gamma_{k,pq}e_{pq}] - G_{k,pq}^{-1}\left\{\dot{F}_{k,pq} + \gamma_{k,pq}[F_{k,pq} + G_{k,pq}i_{k,s}]\right\}. \quad (27)$$

Due to the presence of nearby GFMs or the voltage control capability of the GFL, it is reasonable to assume that $v_{k,o}$ is approximately constant. This observation will simplify the calculation of $\dot{F}_{k,pq}$ and $\dot{G}_{k,pq}$. Further simplification of the above is possible by directly calculating $i_{k,s}^c$ instead of deriving $i_{k,s}^c$ from e_{pq} as shown in the following subsection.

B. WITHOUT POWER FEEDBACK

A power feedback free method of power injection can also be designed under the same paradigm. The references P_k^r and Q_k^r can be tracked under the feed-forward power tracking control $u_{k,pq}$ as,

$$u_{k,pq} = -B_{k,3}^{-1}\left[A_{k,32}v_{k,o} + A_{k,33}i_{k,s} + \gamma_{k,is}(i_{k,s} - i_{k,s}^c)\right], \quad (28)$$

where $\gamma_{k,is} > 0$ is a control gain,

$$i_{k,s}^c = -{A_{k,23}}^{-1}[A_{k,21}i_{k,o}^r + A_{k,22}v_{k,o}] \quad (29)$$

$$i_{k,o}^r = \begin{bmatrix} i_{k,od}^r \\ i_{k,oq}^r \end{bmatrix} = \frac{2}{3}\begin{bmatrix} v_{k,od} & v_{k,oq} \\ v_{k,oq} & -v_{k,od} \end{bmatrix}^{-1}\begin{bmatrix} P_k^r \\ Q_k^r \end{bmatrix}. \quad (30)$$

In (21) and (28) we see the use of similar current control as in (18). This design unifies the GFM and GFL modes of control of the SDI. In the following section, a constraint-enforcing design is developed to restrict, real power, reactive power, voltage, and current during steady-state and transient conditions.

V. CONSTRAINT-ENFORCING CONTROL DESIGN

Although the controls designed above ensure voltage and current tracking, limiting the voltage, real, and reactive power output of the inverter in GFM and GFL modes is important when operating with intermittent renewable energy resources and while maintaining stable grid conditions. Also, transient voltage and current deviations during events like faults, load switching, etc., should be restricted. Therefore, the optimized state-constrained control design principle presented in [12], [14], and [24] is applied to design the operational constraints.

The principle premise behind this form of constraint enforcement is that when an error in either P_k or Q_k or $V_{k,o}$ emerges, u_k should be chosen to reduce this error to zero. Since P_k, Q_k and $V_{k,o}$, are of relative degree 2, we define an error system with second-order dynamics as,

$$\ddot{e} + (\beta_1 + \beta_2)\dot{e} + \beta_1\beta_2 e \leq 0.$$

For P_k we can rewrite the above as,

$$\ddot{\tilde{P}}_k + (\beta_{p1} + \beta_{p2})\dot{\tilde{P}}_k + \beta_{p1}\beta_{p2}\tilde{P}_k \leq 0$$

where $\tilde{P_k} = P_k - \overline{P_k}$. Simplifying the above expression using (4), (5), (6), (8), and (9) we get,

$$G_{k,P}u_{k,c} + E_{k,P} \leq 0. \quad (31)$$

The terms $G_{k,P}$ and $E_{k,P}$ are described in Appendix A. No action is needed if $u_{k,c}$ satisfies the above constraint. Otherwise, we treat (31) as a plane and reflect the outlying point $u_{k,c}$ onto the plane as shown in Fig. 3. To visualize the plane of feasible points we rewrite the above inequality as

$$G_{k,P}^T u_k^T + E_{k,P} = 0, \quad (32)$$

where u_k^T has coordinates in $dq0$ which has the normal

$$\vec{n} = G_{k,p}.$$

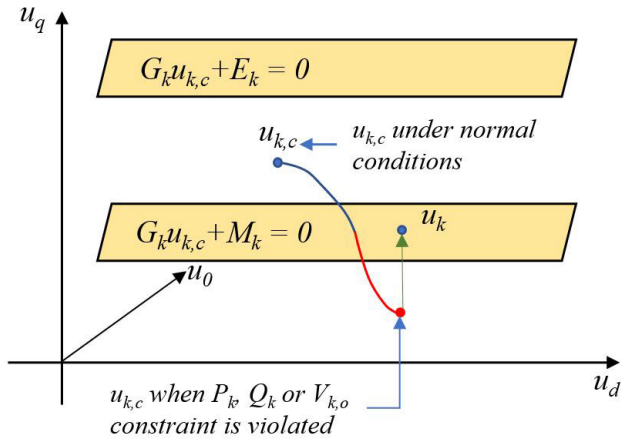

FIGURE 3. Illustration of constraint-enforcing control.

As such, the projection of $u_{k,c}$ onto this plane is u_k, where,

$$u_k^T = u_{k,c} - \lambda G_{k,p}, \quad \lambda \in \Re.$$

Substituting the u_k^T from the above equation into the feasible plane (32) we finally have,

$$u_k = u_{k,c} - \frac{G_{k,p}^T u_{c,k} + E_{P,k}}{G_{k,p}^T G_{k,p}} G_{k,p}.$$

Similarly, for the lower limits of P_k one can find the feasible plane as

$$G_{k,P} u_{k,c} + M_{k,P} \geq 0. \tag{33}$$

for which $\tilde{P}_k = P_k - \underline{P_k}$. Therefore, defining these planes for P_k, Q_k, and V_k we have a set of inequalities that are verified at all times:

$$\begin{cases} G_{k,v} u_{k,c} + E_{k,v} \leq 0 \\ G_{k,v} u_{k,c} + M_{k,v} \geq 0, \end{cases} \quad \begin{cases} G_{k,q} u_{k,c} + E_{k,q} \leq 0 \\ G_{k,q} u_{k,c} + M_{k,q} \geq 0, \end{cases} \tag{34}$$

$$\begin{cases} G_{k,P} u_{k,c} + E_{k,P} \leq 0 \\ G_{k,P} u_{k,c} + M_{k,P} \geq 0, \end{cases} \quad \begin{cases} G_{k,Q} u_{k,c} + E_{k,Q} \leq 0 \\ G_{k,Q} u_{k,c} + M_{k,Q} \geq 0, \end{cases} \tag{35}$$

where matrices $G_{k,v}$, $G_{k,q}$, $G_{k,P}$, $G_{k,Q}$, $E_{k,v}$, $E_{k,q}$, $E_{k,P}$, $E_{k,Q}$, $M_{k,v}$, $M_{k,q}$, $M_{k,P}$, and $M_{k,Q}$ are provided in the appendix A. During the grid-forming phase, voltage constraints are checked with the least priority (first in order) as they are maintained in the tracking control (18). During grid following, the real and reactive power constraints are checked with the least priority as they are maintained in the tracking control (21) or (28).

Although constraints on P_k, Q_k, and $V_{k,o}$ facilitate practical DER operation, a constraint on $I_{k,s}$ is also important to ensure the safe operation of the inverter. This is especially critical during faults when GFM/GFL control or P_k, Q_k, and $V_{k,o}$ constraints might force the current to exceed the rated limits. Since dynamics of $i_{k,s}$ are of relative degree one, the formulation of the constraint on $i_{k,s}$ is simply performed by using (21) or (28) for the GFL mode and (18) for the GFM mode, with the exception that the reference current $i_{k,s}^c$ is fixed at its maximum rated value. Details of the current constraints are included in Appendix B.

VI. INTERCHANGE BETWEEN GFM AND GFL MODES

In the proposed controls, the mode of operation of the inverter can be toggled manually or automatically. When automatic toggling is enabled, the operating mode is decided by a trigger logic as follows:

$$\rho_k^g(t) = \begin{cases} 1 & \text{if the } k^{th} \text{ DG's on-off switch} = 0 \\ 1 & \text{if } \overline{P_k} = \overline{P}_{\mathcal{N}_k} \\ 1 & \text{if } V_{k,b}^a \in [\underline{V},\ \overline{V}] \\ 0 & \text{otherwise} \end{cases} \tag{36}$$

where $\overline{P}_{\mathcal{N}_k} = \max[\overline{P_k},\ \overline{P_j} : \forall j \in \mathcal{N}_k(t)]$, $\rho_k^g(t)$ is true (or 1) for the GFM mode and false (or 0) for the GFL mode. Signal $\rho_k^g(t)$ is further processed by using a low pass filter to remove oscillations and a threshold to generate true or false commands.

The first condition ensures that the inverter always starts up as a GFM inverter. This ensures that supply to local loads is retained before synchronization or after disconnection from the remaining network. The second condition ensures that the DG with the largest $\overline{P_k}$ in the neighborhood (explained next) is the GFM. This condition also ensures that there is at least one DG as GFM in the neighborhood at all times. Finally, the average of neighborhood DG bus voltages $V_{k,b}^a$ is checked against the upper and lower tolerances of ($\underline{V}$, $\overline{V}$) 1.05 p.u. and 0.95 p.u., respectively, in compliance with the existing standards [25], where $V_{k,b}^a$ is formulated as:

$$V_{k,b}^a = \frac{1}{1 + |\mathcal{N}_k|} \left[V_{k,b} + \sum_{j \in \mathcal{N}_k} V_{j,b} \right]. \tag{37}$$

Quantities $V_{k,b}^a$ and $\overline{P}_k$ are defined in terms of a neighborhood around the k^{th} DG. In a microgrid with N DGs, the local communication among the DGs and each DG's neighbors are characterized by a binary matrix as [23]:

$$S(t) = \begin{bmatrix} 1 & s_{12}(t) & \cdots & s_{1N}(t) \\ s_{21}(t) & 1 & \cdots & s_{2N}(t) \\ \vdots & \vdots & \vdots & \vdots \\ s_{N1}(t) & s_{N2}(t) & \cdots & 1 \end{bmatrix}, \tag{38}$$

Here $\{s_{kj} = 1 : j, k \in \mathcal{N}\}$ if the jth DG sends and receives information to the k^{th} DG. The diagonal elements of S are always 1. Although S is represented as a matrix, the k^{th} DG only knows the k^{th} row of the matrix. As such, if $\mathcal{N}$ is the index set of DGs, the neighborhood of the k^{th} DG is defined by

$$\mathcal{N}_k(t) = \{j \in \mathcal{N} :\ s_{kj}(t) = 1\ \}.$$

VII. SIMULATION AND IMPLEMENTATION RESULTS

Four simulation case studies are included in this section. Case 1 is a hardware-platform-based test. Case 2 is an Opal-RT-based real-time simulation. Case 2 involves a single

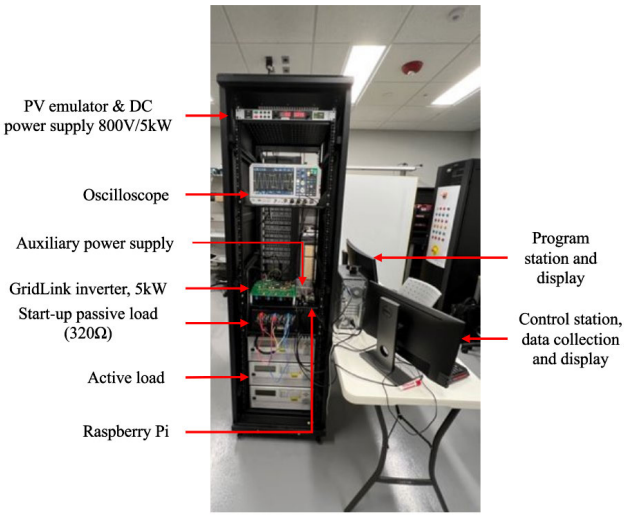

FIGURE 4. Experimental platform with GridLink inverter.

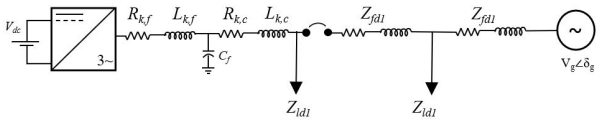

FIGURE 5. Single inverter system for case 1.

TABLE 1. Parameters of the test systems.

Base Values and Parameter Values			
f_0	60Hz	$R_{k,f}$	0.1 Ω
V_0	$\sqrt{2}$*277 V	$L_{k,f}$	1.35 mH
V_{dc}	1000 V	$R_{k,c}$	0.03 Ω
S_k	$1.2\overline{P}_k$	$L_{k,c}$	0.35 mH
$\overline{P}_k$	$[5,5,5,5]^\top$ kW	C_k	50 μF
Z_{fd1}	0.115 +j0.1Ω	Z_{ld1}	15 Ω
Z_{fd2}	0.175 +j0.58Ω	Z_{ld2}	10 + j5.7Ω

inverter system as shown in Fig. 5. Cases 3 and 4 are microgrid test cases involving 4 DGs as shown in Fig. 6. Cases 3 and 4 are Simulink environment-based tests. The 4-DG system was derived from [26]. The parameters of these systems are given in Table 1.

A brief summary of the operating principle of the DGs in the designed paradigm is as follows. When operated in the GFM mode, SDIs use their primary voltage and frequency control, (18) and (16) to establish voltage and frequency. When operated in the GFL mode, SDIs use their primary power control (with or without feedback) to inject the desired power, and their primary frequency control to track the grid frequency. Whenever operational constraints are to be strictly enforced (for either GFM or GFL modes), the real-time constraint-enforcement controls (34), (35), (A.8), (A.9), (A.10) are applied.

A. CASE 1: HARDWARE-BASED DEMONSTRATION OF THE PROPOSED GFM CONTROLS ON GRIDLINK INVERTER TESTBED

Fig. 4 shows the experimental setup of Siemens' GridLink inverter [27], PV emulator, and 3-phase AC loads. The inverter is directly interfaced with a resistive load. The

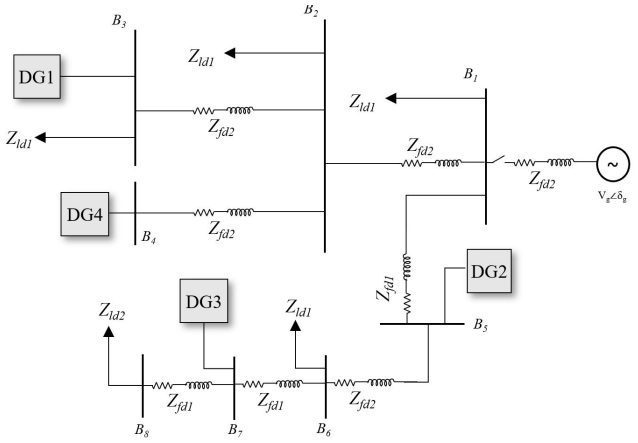

FIGURE 6. Isolated 4-DG microgrid.

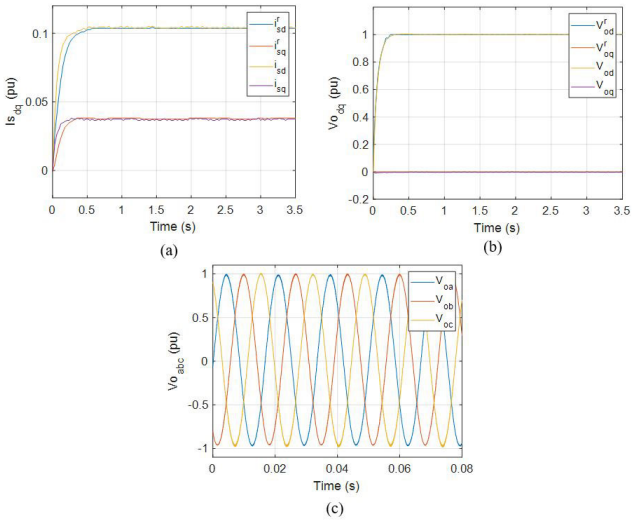

FIGURE 7. Case 1 hardware implementation results: (a) current loop output; (b) voltage loop output; and (c) inverter AC output voltage.

GridLink inverter is a 3-phase, three-level active neutral-point-clamped (ANPC) converter. The GridLink inverter is an SDI that allows us to implement any specific control by programming the controls in Simulink and then deploying the resulting C codes through a Joint Test Action Group (JTAG) programmer. The voltage reference and on/off commands to the inverter are sent in real-time via a RaspberryPi and CAN communication protocol.

The proposed GFM control is implemented and validated using the GridLink testbed in Fig. 4. Specifically, Fig. 7 shows the dq components of current reference $i^r_{k,s}$, current $i_{k,s}$, voltage reference $v^r_{k,o}$, and voltage $v_{k,o}$, as well as 3-phase AC output voltages $v_{o,abc}(t)$. The results clearly show that the proposed GFM primary control achieves grid-forming with very good tracking of current and voltage references in the presence of high-frequency switching dynamics.

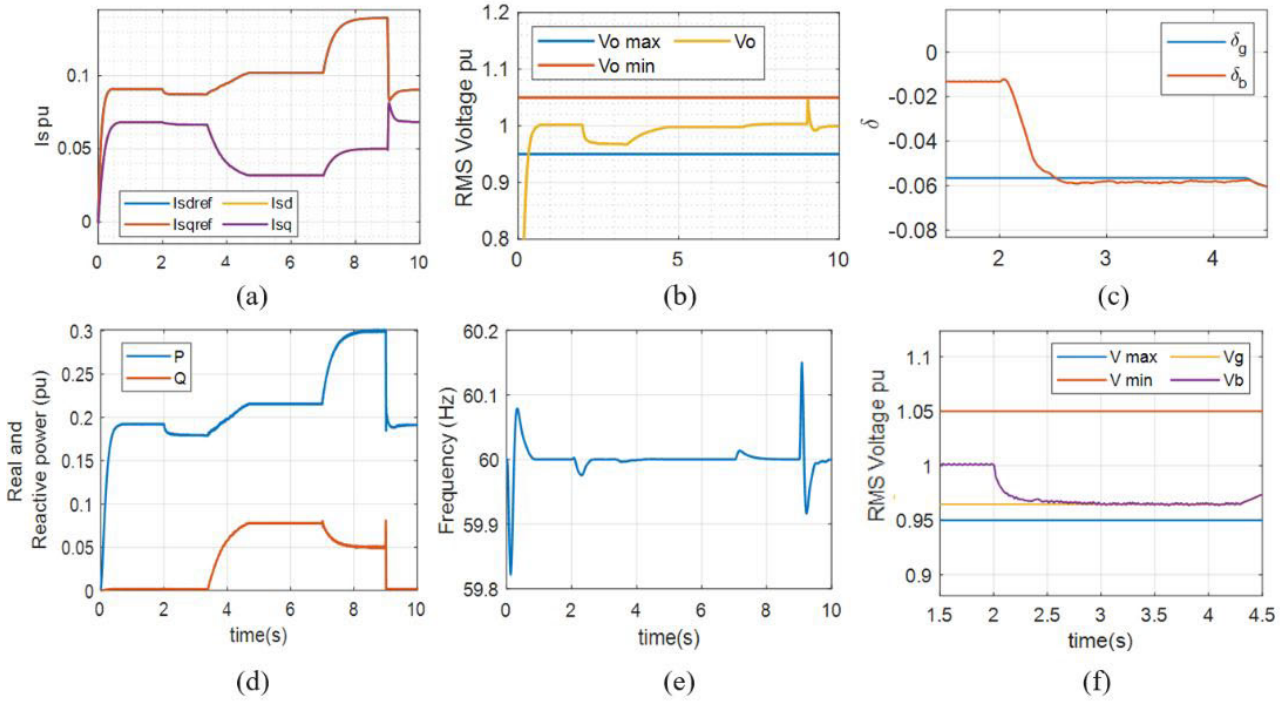

FIGURE 8. Case 2 Opal-RT based simulation of one-inverter system (a) current tracking, (b) voltage, (c) angle tracking during synchronization, (d) real and reactive power, (e) frequency, and (f) voltage magnitude during synchronization.

The main challenges for the successful implementation of the controls were: a) the correction of onboard sensors for accurate feedback via approximate correction gains, b) filter design and implementation for filtering the feedback signals, and c) balancing of DC voltages with separate DC stage balancing control under different loading conditions.

B. CASE 2: GFM/GFL MODE TRANSITION, SYNCHRONIZATION, AND SUDDEN DISCONNECTION

This test considers the system in Fig. 5 where the SDI inverter is chosen to be the IGBT-based 6-switch 3-phase bridge from the ARTEMiS library in RT-Lab using Opal-RT cores [28]. The effectiveness of the proposed controls is shown in Fig. 8, in the presence of high-frequency harmonics. The only addition is a low-pass filter of 95Hz cut-off frequency on the feedback measurements. Another point elaborated by this test is the smooth interchange from GFM to GFL mode. A sequence of events is simulated as follows:

- *Grid-forming over* $t \in [0\ 2]s$: During this phase, the grid voltage is formed with a local load. Real and reactive powers are injected to bring up the voltage and frequency to the required 1 p.u. and 60 Hz, respectively. Voltage constraints are activated with a delay to allow the voltage tracking control to raise the voltage gradually.
- *Synchronization and connection for* $t \in [2\ 7]s$: The SDI starts to synchronize itself to the voltage at the point of common coupling (PCC) at $t = 2$s. Fig. 8c displays the outcome of the angle control. A small dead zone is applied to the angle error to prevent excessive control action at the end. Due to this angle synchronization, a slight frequency transient can also be observed in Fig. 8(e). Fig. 8(f) shows the action of the voltage control as it attempts to make $V_{k,b}$ match up with the voltage magnitude at PCC. After the breaker closes, the SDI (still in the GFM mode) restores its terminal voltage to 1 p.u., as shown in Fig. 8(b).
- *Switch from GFM to GFL during* $t \in [7\ 9]s$: At $t = 7$s, the SDI is manually transitioned into the GFL mode and tracks fixed P_k and Q_k references of 0.3 p.u. and 0.05 p.u., respectively. As power injections are achieved, there are small transients in voltage and frequency as expected.
- *Sudden Islanding*: At $t = 9$s, the breaker suddenly opens. Based on the difference in the voltage and angles on each side of the breaker, the SDI transitions back to the GFM mode. A sudden spike in voltage is confined by the constraint-enforcing voltage control. The real and reactive power injections return to pre-synchronization values. Since this is a sudden transition from GFL to GFM mode, transients are seen but are arrested by the constraint-enforcing control.

Note, that the above case displays an extreme case of breaker failure. If the grid disconnection would be planned, the DG would first transition to GFM, reduce power from the grid using angle control and then disconnect the breaker. This would have led to a smoother disconnection.

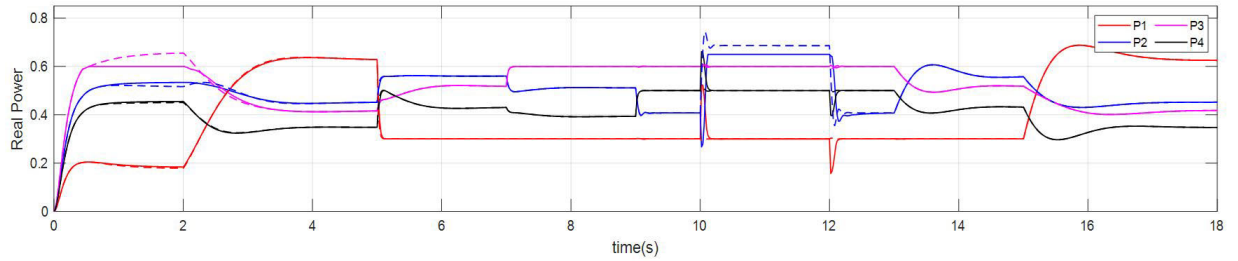

(a)

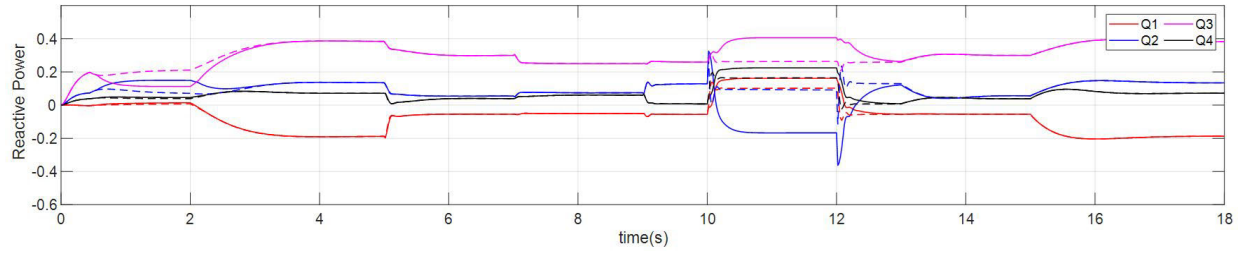

(b)

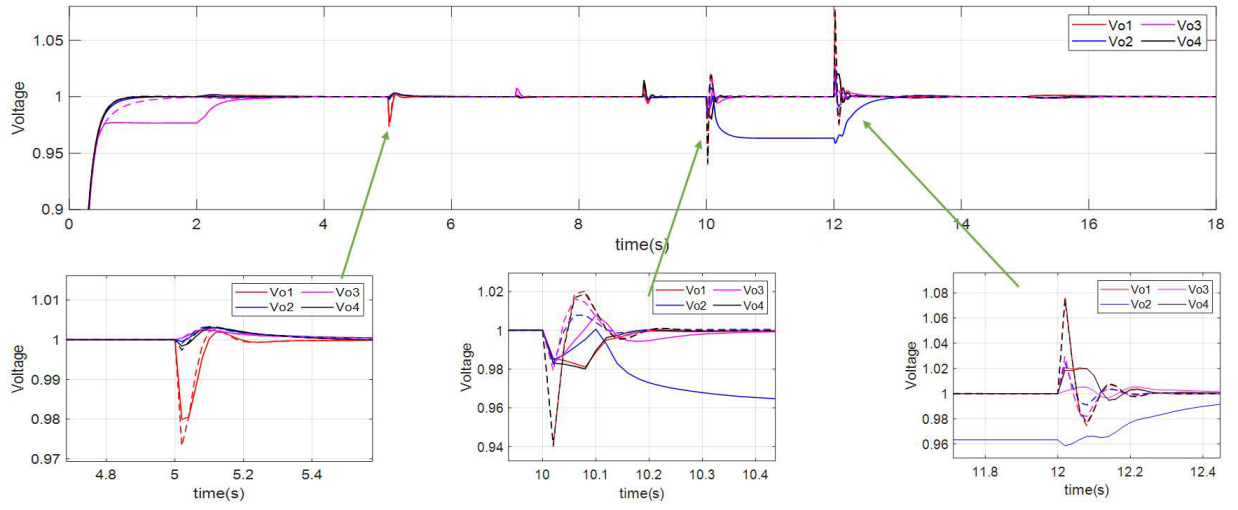

(c)

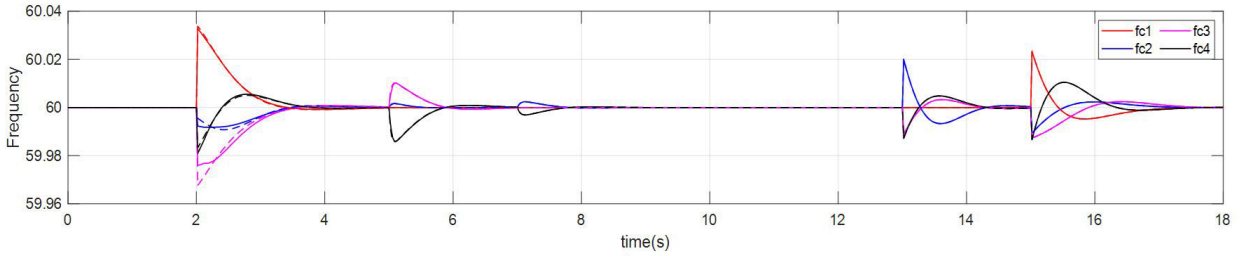

(d)

FIGURE 9. Case 3 with four DG microgrid test cases (a) real power, (b) reactive power, (c) voltage, and (d) frequency. Dashed lines indicate the case without constraint-enforcing control.

C. CASE 3: MULTIPLE DG SYNCHRONOUS START, MODE TRANSITIONS, AND LOAD CHANGES IN A MICROGRID

This case study considers the microgrid shown in Fig. 6. While DG 2 is intentionally held as a GFM inverter throughout the simulation, the other DGs transition between GFL and GFM modes at preset times that are set before the simulation begins. To show the effectiveness of the angle controls, a real power utilization ratio ($P_k/\overline{P}_k$) sharing scheme using

the technique designed in [29] is used to share real power between GFM inverters. The case study is divided into the following five-time intervals during which disturbances are simulated, and the results are presented in Fig. 9. For comparative illustration, the results with and without constraint-enforcing control are represented by the solid line and the dashed line, respectively.

- *Synchronous black start over* $t \in [0\ \ 2]s$: All DGs start as GFM, and their power injections bring their terminal voltages to 1 p.u. Should one (or more) of the GFM inverters have limited power available, say that DG 3 is subject to the real-power limit of.6 p.u., the constraint-enforcing control would stop lifting the terminal voltage once the power limit is reached while unconstrained primary control always achieves precise voltage tracking.
- *Angle control over* $t \in [2\ \ 5]s$: A load-sharing scheme produces an angle reference for each of the DGs. By tracking these references through a temporary change in frequency, DGs adjust their output. As such, DG 3 lowers its injection from its power limit, while other DGs adapt accordingly. While real and reactive power injections are changed, the voltages are well-regulated and remain constant.
- *Transitions from GFM to GFL during* $t \in [5\ \ 10]s$: During this period, DGs 1, 3, and 4 transitions to the GFL mode at predetermined time instants of $t = 5$, 7, and 9s to track fixed references of real power $P_k = .3$, .6, and .5 p.u., respectively, while reactive power is controlled by a Q-V control mechanism to maintain 1 p.u. terminal voltage. Two key observations can be made; a) the designed GFL controls are accurate, b) voltage constraints limit the voltage dips during transients and c) GFMs are seen to respond rapidly to load and generation imbalance.
- *Load addition and removal during* $t \in [10\ \ 12]s$: A load of $0.285 - 0.26j$ p.u. is suddenly applied and removed at 10s and 12s, respectively, at bus B2. GFM DG 2 would pick up the load change but, as its active power reaches.65 p.u. limit, its nodal voltage drops. Concurrently, one can also think of it as the lowering of the terminal voltage of the DG to lower the terminal load and hence the power output.
- *Transitions from GFL to GFM during* $t \in [12\ 18]s$: Load removal at $t = 12s$ allows GFM DG 2 to return to its pre-disturbance condition. Subsequently, GFL inverters 1, 3, and 4 transition back to GFM at preset time instants of $t = 15$, 13, 13s, respectively. In their GFM mode, the DGs resume angle reference tracking as evident in Fig. 9d. Note, that no mode transition transients were observed. Unlike case 2, the transition was not triggered by a grid disconnection type or similar event and operating conditions before and during the mode change were nominal.

D. CASE 4: MULTIPLE DG, ASYNCHRONOUS STARTS, AUTOMATIC MODE TOGGLING, SINGLE LINE TO GROUND (SLG) FAULT, THREE PHASE TO GROUND (3LG) FAULT, AND INDUCTION MOTOR START-UP IN THE MICROGRID

In this case study, the ability of inverters to withstand and to ride - through power system transients is investigated using the microgrid in Fig. 6. Four events are simulated and results are presented in Fig. 10. Here, condition 2 of (36) is disabled and instead, DG1 and DG2 are intentionally held as GFM throughout the simulation. DGs 3 and 4 are free to toggle automatically between GFM and GFL modes.

- *Asynchronous black start over* $t \in [0\ 5]s$: DG 1 starts up at $t = 0$ and while DGs 2, 3, and 4 begin their synchronization at preset-times of $t = 1$s, 2s, 3s respectively. Once the frequency, angle, and voltage magnitude are matched on either side of the breaker, the breaker turns on. Fig. 10a shows that constraint-enforcing control limits DG injections to their maximum available values. As such, the voltage levels around 1 p.u. are finally achieved after DGs 3 and 4 are synchronized. Per conditions 1 and 3 of (36), DG 3 starts up as GFM but transitions to GFL only after a delay required to boost average voltages to 1pu. Also, in accordance with conditions 1 and 3 of (36), DG4 is GFM while synchronizing but transitions to GFL immediately after the close of its breaker.
- *Single-line-to-ground (SL2G) fault for* $t \in [5\ 7]s$: A SL2G fault is applied on phase A at bus B2 near DG 4 (GFL) and DG 1 (GFM) at time $t = 5$s for a period of 3 cycles. The positive sequence voltage drops during the fault and condition 3 of (36) is violated. As such, GFL inverters DG3 and DG4 transition to GFM and help keep up the voltage. In addition, the system becomes unbalanced, and the $dq0$ feedback measurement components and corresponding power injections become oscillatory. The constraint-enforcing control limits the magnitude of these oscillations to $\overline{P}_k$ and $\overline{Q}_k$.
- *Three-line-to-ground (3L2G) fault during* $t \in [7\ 9]s$: A 3L2G fault is applied at bus B4 at $t = 7$s for a period of 3 cycles, and the proximity of the fault to the DGs is in the order of DG 4, DG 1, DG 2, and DG 3. During the fault, voltages sag, and condition 3 of (36) is violated. Grid-forming is disrupted, GFL DGs automatically transition to GFM, and all four GFM DGs attempt to increase their voltages. It is shown in Fig. 10c that the constraint-enforcing control limits the current magnitude to 1.2 p.u. and real and reactive power injections to $\overline{P}_k$ and $\overline{Q}_k$.
- *Induction motor start during* $t \in [9\ 11]s$: An induction motor with a centrifugal load rated at .3 p.u. at 1 p.u. speed is placed on bus B2. When the induction motor starts at $t = 9$s, it draws a high current and a lot of reactive power. Fig. 10 shows that the proposed constraint-enforcing control ensures observation of the maximum power ratings of $\overline{S}_k$, $\overline{P}_k$, and $\overline{Q}_k$. This prevents

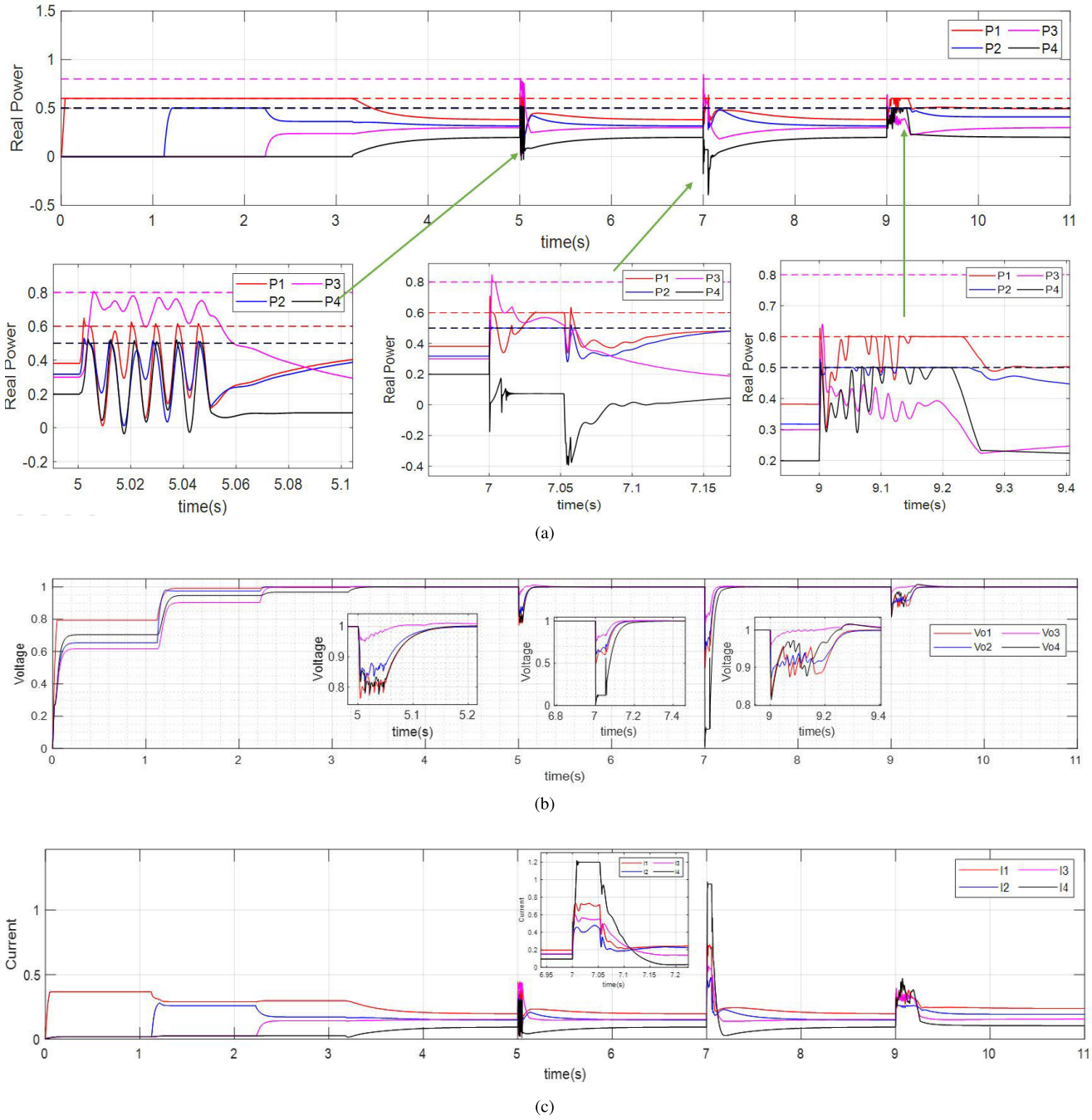

FIGURE 10. Case 4 with four DG microgrid test case with asynchronous start, SL2G fault, 3L2G fault and induction motor start-up, showing (a) real power, (b) voltage, and (c) current.

inverter damage. However, the trade-off is that the motor start-up takes slightly longer, and the voltage sag is slightly deeper. Similar observations in mode change are made here. Since all 4 DGs communicate with each other, the average voltage drops below the threshold, and all GFL DGs transition to GFM to boost their terminal voltage.

In the case of every disturbance, once the disturbance is removed, the voltage and frequency recover, the grid-forming trigger returns to true, and DGs 3 and 4 transition back to the GFL mode.

VIII. CONCLUSION

In this paper, a nonlinear and recursive design of unified GFM/GFL controls is presented, and the proposed controls are synthesized in closed form. The proposed approach guarantees to track performance in both GFM and GFL modes and also allows seamless switching between the two.

Since DERs often have limited capacity and available power, both GFM and GFL controls need to observe their power and current constraints. Simultaneously, reliable grid operation requires that frequencies and voltages stay within an acceptable range. To meet these operational constraints, the GFM/GFL tracking controls are embedded with a state-constraint-enforcing mechanism that follows the same recursive design principle. Also, an automatic mode toggling scheme has been provided that enables the SDI to toggle between GFM and GFL modes. The effectiveness of the proposed GFM/GFL controls and their constraint-enforcing capabilities are demonstrated through mathematical analysis, simulation case studies, and experimental implementation using GridLink software-defined inverters. Future work will focus on the analysis and design of more sophisticated automated mode toggling mechanisms along with DC side controls.

APPENDIX A
EXPRESSIONS OF THE MATRICES

The four sets of matrices in Section V are explicitly defined as follows:

$$\begin{cases} G_{k,v} = \dfrac{1}{V_{k,o}} v_{k,o}^{\top} A_{k,23} B_{k,3}, \\ E_{k,v} = F_{k,v} - \beta_{v1}\beta_{v2} V_0 (1 + \Delta_v) \\ M_{k,v} = F_{k,v} - \beta_{v1}\beta_{v2} V_0 (1 - \Delta_v), \end{cases} \tag{A.1}$$

$$\begin{cases} G_{k,P} = \dfrac{3}{2} i_{k,o}^{\top} A_{k,23} B_{k,3}, \\ E_{k,P} = F_{k,P} - \ddot{\overline{P}}_k - (\beta_{p1} + \beta_{p2}) \dot{\overline{P}}_k - \beta_{p1}\beta_{p2} \overline{P}_k \\ M_{k,P} = F_{k,P} - \ddot{\underline{P}}_k - (\beta_{p1} + \beta_{p2}) \dot{\underline{P}}_k - \beta_{p1}\beta_{p2} \underline{P}_k, \end{cases} \tag{A.2}$$

$$\begin{cases} G_{k,q} = \begin{bmatrix} 0 & 1 \end{bmatrix}, \\ E_{k,q} = -\dfrac{2V_0 \epsilon_v}{v_{k,dc}} \\ M_{k,q} = \dfrac{2V_0 \epsilon_v}{v_{k,dc}}, \end{cases} \tag{A.3}$$

$$\begin{cases} G_{k,Q} = \dfrac{3}{2} i_{k,o}^{\top} H_q A_{k,23} B_{k,3} \\ E_{k,Q} = F_{k,Q} - \ddot{\overline{Q}}_k - (\beta_{q1} + \beta_{q2}) \dot{\overline{Q}}_k - \beta_{q1}\beta_{q2} \overline{Q}_k \\ M_{k,Q} = F_{k,Q} + \ddot{\underline{Q}}_k + (\beta_{q1} + \beta_{q2}) \dot{\underline{Q}}_k + \beta_{q1}\beta_{q2} \underline{Q}_k, \end{cases} \tag{A.4}$$

where β_{v1}, β_{v2}, β_{p1}, β_{p2}, β_{p3}, β_{q1}, β_{q2}, and β_{q3} are positive gains, and

$$\begin{aligned} F_{k,1} &= A_{k,11} i_{k,o} + A_{k,12} v_{k,o} + D_{k,1} v_{k,b}, \\ F_{k,2} &= A_{k,21} i_{k,o} + A_{k,22} v_{k,o} + A_{k,23} i_{k,s}, \\ F_{k,v} &= -\frac{1}{V_{k,o}^3} (v_{k,o}^{\top} F_{k,2})^2 + \frac{1}{V_{k,o}} \|F_{k,2}\|^2 \\ &\quad + \frac{1}{V_{k,o}} v_{k,o}^{\top} A_{k,21} F_{k,1} + \frac{1}{V_{k,o}} v_{k,o}^{\top} A_{k,22} F_{k,2} \\ &\quad + \frac{1}{V_{k,o}} v_{k,o}^{\top} A_{k,23} [A_{k,32} v_{k,o} + A_{k,33} i_{k,s}] \\ &\quad + (\beta_{v1} + \beta_{v2}) \frac{1}{V_{k,o}} v_{k,o}^{\top} F_{k,2} + \beta_{v1}\beta_{v2} V_{k,o} \end{aligned} \tag{A.5}$$

$$\begin{aligned} F_{k,P} &= \frac{3}{2} \big[v_{k,o}^{\top} (A_{k,11} F_{k,1} + A_{k,12} F_{k,2} + D_{k,1} \dot{v}_{k,b}) \\ &\quad + F_{k,1}^{\top} F_{k,2} + i_{k,o}^{\top} (A_{k,21} F_{k,1} + A_{k,22} F_{k,2} \\ &\quad + A_{k,23} A_{k,32} v_{k,o} + A_{k,23} A_{k,33} i_{k,s}) \big] \\ &\quad + \frac{3}{2} (\beta_{p1} + \beta_{p2}) [F_{k,1}^{\top} v_{k,o} + i_{k,o}^{\top} F_{k,2}] \\ &\quad + \beta_{p1}\beta_{p2} P_k \end{aligned} \tag{A.6}$$

$$\begin{aligned} F_{k,Q} &= \frac{3}{2} \big[- v_{k,o}^{\top} H_q (A_{k,11} F_{k,1} + A_{k,12} F_{k,2} + D_{k,1} \dot{v}_{k,b}) \\ &\quad + F_{k,1}^{\top} H_q F_{k,2} + i_{k,o}^{\top} H_q (A_{k,21} F_{k,1} + A_{k,22} F_{k,2} \\ &\quad + A_{k,23} A_{k,32} v_{k,o} + A_{k,23} A_{k,33} i_{k,s}) \big] \\ &\quad + \frac{3}{2} (\beta_{q1} + \beta_{q2}) [F_{k,1}^{\top} H_q v_{k,o} + i_{k,o}^{\top} H_q F_{k,2}] \\ &\quad + \beta_{q1}\beta_{q2} Q_k. \end{aligned} \tag{A.7}$$

APPENDIX B
CURRENT CONSTRAINED CONTROL

Consider $\overline{I}_k$ is the inverter's maximum peak current rating as defined in (13). If either $i_{k,sd}$ or $i_{k,sq}$ or both exceeds the current limit, they will be saturated. For example, if $i_{k,sq}$ is the main item that exceeds the limit, the following saturation is applied:

$$i_{k,sq}^{nc} = \begin{cases} \text{sign}(i_{k,sq}^{c}) \times \overline{I}_k, & \text{if } |i_{k,s}^{c}| > \overline{I}_k \\ i_{k,sq}^{c}, & \text{otherwise} \end{cases} \tag{A.8}$$

where $i_{k,sq}^{nc}$ is the new q-axis reference current for the current tracking loop. When (and only if) the above condition is executed, current $i_{k,sd}^{c}$ is recalculated as follows:

$$i_{k,sd}^{nc} = \sqrt{\overline{I}_k^2 - (i_{k,sq}^{nc})^2} \tag{A.9}$$

Considering $\frac{di_{k,s}^{nc}}{dt} = 0$, the control $u_{k,pq}$ or $u_{k,v}$ can modified to

$$u_k = \begin{cases} -B_{k,3}^{-1} [A_{k,32} v_{k,o} + A_{k,33} i_{k,s} + (i_{k,s} - i_{k,s}^{nc})] \\ \quad \text{if } ||I_s|| > I_{max} \\ (18) \text{ or } (28) \text{ or } (21) \quad \text{otherwise} \end{cases} \tag{A.10}$$

where $\underline{I}_{k,s}$ is the lower bound (set to be $-\overline{I}_k$).

REFERENCES

[1] Z. Li, C. Zang, P. Zeng, H. Yu, S. Li, and J. Bian, "Control of a grid-forming inverter based on sliding-mode and mixed H_2/H_∞ control," *IEEE Trans. Ind. Electron.*, vol. 64, no. 5, pp. 3862–3872, May 2017.

[2] X. Quan, A. Q. Huang, and H. Yu, "A novel order reduced synchronous power control for grid-forming inverters," *IEEE Trans. Ind. Electron.*, vol. 67, no. 12, pp. 10989–10995, Dec. 2020.

[3] J. Chen, F. Prystupczuk, and T. O'Donnell, "Use of voltage limits for current limitations in grid-forming converters," *CSEE J. Power Energy Syst.*, vol. 6, no. 2, pp. 259–269, Jun. 2020.

[4] W. Du, F. K. Tuffner, K. P. Schneider, R. H. Lasseter, J. Xie, Z. Chen, and B. Bhattarai, "Modeling of grid-forming and grid-following inverters for dynamic simulation of large-scale distribution systems," *IEEE Trans. Power Del.*, vol. 36, no. 4, pp. 2035–2045, Aug. 2021.

[5] P. J. Hart, R. H. Lasseter, and T. M. Jahns, "Coherency identification and aggregation in grid-forming droop-controlled inverter networks," *IEEE Trans. Ind. Appl.*, vol. 55, no. 3, pp. 2219–2231, May 2019.

[6] T. L. Vandoorn, B. Meersman, J. D. M. De Kooning, and L. Vandevelde, "Analogy between conventional grid control and islanded microgrid control based on a global DC-link voltage droop," *IEEE Trans. Power Del.*, vol. 27, no. 3, pp. 1405–1414, Jul. 2012.
[7] B. B. Johnson, S. V. Dhople, A. O. Hamadeh, and P. T. Krein, "Synchronization of parallel single-phase inverters with virtual oscillator control," *IEEE Trans. Power Electron.*, vol. 29, no. 11, pp. 6124–6138, Nov. 2014.
[8] M. Sinha, F. Dörfler, B. B. Johnson, and S. V. Dhople, "Uncovering droop control laws embedded within the nonlinear dynamics of van der Pol oscillators," *IEEE Trans. Control Netw. Syst.*, vol. 4, no. 2, pp. 347–358, Jun. 2017.
[9] M. A. Awal and I. Husain, "Unified virtual oscillator control for grid-forming and grid-following converters," *IEEE J. Emerg. Sel. Topics Power Electron.*, vol. 9, no. 4, pp. 4573–4586, Aug. 2021.
[10] B. B. Johnson, M. Sinha, N. G. Ainsworth, F. Dörfler, and S. V. Dhople, "Synthesizing virtual oscillators to control islanded inverters," *IEEE Trans. Power Electron.*, vol. 31, no. 8, pp. 6002–6015, Aug. 2016.
[11] M. A. Awal, H. Yu, I. Husain, W. Yu, and S. M. Lukic, "Selective harmonic current rejection for virtual oscillator controlled grid-forming voltage source converters," *IEEE Trans. Power Electron.*, vol. 35, no. 8, pp. 8805–8818, Aug. 2020.
[12] Y. Xu, Z. Qu, and J. Qi, "State-constrained grid-forming inverter control for robust operation of ac microgrids," in *Proc. Eur. Control Conf.*, Saint Petersburg, Russia, May 2020, pp. 471–474.
[13] N. Pogaku, M. Prodanovic, and T. C. Green, "Modeling, analysis and testing of autonomous operation of an inverter-based microgrid," *IEEE Trans. Power Electron.*, vol. 22, no. 2, pp. 613–625, Mar. 2007.
[14] R. Harvey, Z. Qu, and T. Namerikawa, "An optimized input/output-constrained control design with application to microgrid operation," *IEEE Control Syst. Lett.*, vol. 4, no. 2, pp. 367–372, Apr. 2020.
[15] H. Xin, Z. Qu, J. Seuss, and A. Maknouninejad, "A self-organizing strategy for power flow control of photovoltaic generators in a distribution network," *IEEE Trans. Power Syst.*, vol. 26, no. 3, pp. 1462–1473, Aug. 2011.
[16] A. Maknouninejad and Z. Qu, "Realizing unified microgrid voltage profile and loss minimization: A cooperative distributed optimization and control approach," *IEEE Trans. Smart Grid*, vol. 5, no. 4, pp. 1621–1630, Jul. 2014.
[17] V. Nasirian, Q. Shafiee, J. M. Guerrero, F. L. Lewis, and A. Davoudi, "Droop-free distributed control for AC microgrids," *IEEE Trans. Power Electron.*, vol. 31, no. 2, pp. 1600–1617, Feb. 2016.
[18] H. Zhang, S. Kim, Q. Sun, and J. Zhou, "Distributed adaptive virtual impedance control for accurate reactive power sharing based on consensus control in microgrids," *IEEE Trans. Smart Grid*, vol. 8, no. 4, pp. 1749–1761, Jul. 2017.
[19] A. Bidram, V. Nasirian, A. Davoudi, and F. L. Lewis, *Cooperative Synchronization in Distributed Microgrid Control*. Berlin, Germany: Springer, 2017.
[20] L. M. Wieserman, S. F. Graziani, T. E. McDermott, R. C. Dugan, and Z.-H. Mao, "Test-based modeling of photovoltaic inverter impact on distribution systems," in *Proc. IEEE 46th Photovoltaic Specialists Conf. (PVSC)*, Jun. 2019, pp. 2977–2983.
[21] L. M. Wieserman, "Developing a transient photovoltaic inverter model in OpenDSS using the Hammerstein–Wiener mathematical structure," Ph.D. dissertation, Elect. Comput. Eng., Univ. Pittsburgh, Pittsburgh, PA, USA, 2016.
[22] H. K. Khalil, *Nonlinear Systems*. Upper Saddle River, NJ, USA: Prentice-Hall, 2002.
[23] Z. Qu, *Cooperative Control of Dynamical Systems*. Berlin, Germany: Springer, 2009.
[24] R. Harvey, Z. Qu, and T. Namerikawa, "Coordinated optimal control of constrained DERs," in *Proc. IEEE Conf. Control Technol. Appl. (CCTA)*, Aug. 2018, pp. 224–229.
[25] *IEEE Standard for Interconnection and Interoperability of Distributed Energy Resources With Associated Electric Power Systems Interfaces*, Standard 1547, 2018.
[26] D. K. Nichols, J. Stevens, R. H. Lasseter, J. H. Eto, and H. T. Vollkommer, "Validation of the CERTS microgrid concept the CEC/CERTS microgrid testbed," in *Proc. IEEE Power Eng. Soc. Gen. Meeting*, Montreal, QC, Canada, 2006, p. 3, doi: 10.1109/PES.2006.1709248.
[27] *DoE Inverter Control Project*. Accessed: Oct. 24, 2022. [Online]. Available: https://www.ece.ucf.edu/ qu/doe-inverter-control/
[28] *Advanced Real-Time Electromagnetic Simulation Solver for the Simscape Electrical ToolBox*. Accessed: Oct. 11, 2022. [Online]. Available: https://www.opal-rt.com/solver/
[29] G. Marasini, Z. Qu, S. Nag, and Y. Xu, "Distributed secondary control of grid-forming inverters and AC microgrids: Impacts of voltage feedback choices," in *Proc. North Amer. Power Symp. (NAPS)*, Oct. 2022, pp. 1–6.

SOUMYADEEP NAG (Member, IEEE) received the Ph.D. degree in electrical engineering from Baylor University, Waco, TX, USA, in December 2020. Currently, he is a Postdoctoral Scholar with the Research Center on Energy Systems, University of Central Florida. His research interest includes the control and grid integration of inverter-based resources.

ZHIHUA QU (Fellow, IEEE) received the Ph.D. degree in electrical engineering from the Georgia Institute of Technology, Atlanta, in June 1990. Since then, he has been with the University of Central Florida (UCF), Orlando, where he is currently a Pegasus Professor, the Thomas J. Riordan and Herbert C. Towle Chair, and the Founding Director of the RISES University Research Center on Energy Systems. His area of expertise is power systems and control.

YING XU (Member, IEEE) received the B.Eng., M.Eng., and Ph.D. degrees from the Harbin Institute of Technology, China, in 2003, 2005, and 2009, respectively. From 2009 to 2017, he was a Senior Engineer with the North China Grid Dispatching and Control Center. He was a Postdoctoral Researcher with the Department of Electrical and Computer Engineering, University of Central Florida (UCF), USA. His main research interests and experience include power system analysis, system modeling and control, big-data implementation in power systems, cooperative control, and distributed optimization for networked systems.